

Article

Computational Design of Inhibitors Targeting the Catalytic β Subunit of *Escherichia coli* F₀F₁-ATP Synthase

Luis Pablo Avila-Barrientos ^{1,†}, Luis Fernando Cofas-Vargas ^{1,†}, Guillermin Agüero-Chapin ^{2,3}, Enrique Hernández-García ¹, Sergio Ruiz-Carmona ^{4,†}, Norma A. Valdez-Cruz ⁵, Mauricio Trujillo-Roldán ⁵, Joachim Weber ⁶, Yasser B. Ruiz-Blanco ^{1,7,*}, Xavier Barril ^{8,9} and Enrique García-Hernández ^{1,*}

- ¹ Instituto de Química, Universidad Nacional Autónoma de México, Ciudad Universitaria, Ciudad de México 04510, Mexico; lpablo@comunidad.unam.mx (L.P.A.-B.); fcofas@comunidad.unam.mx (L.F.C.-V.); enrique.hernandez@iquimica.unam.mx (E.H.-G.)
- ² CIMAR/CIIMAR, Centro Interdisciplinar de Investigação Marinha e Ambiental, Universidade do Porto, Terminal de Cruzeiros do Porto de Leixões, Av. General Norton de Matos, s/n, 4450-208 Porto, Portugal; gchapin@ciimar.up.pt
- ³ Departamento de Biologia, Faculdade de Ciências, Universidade do Porto, Rua do Campo Alegre, 4169-007 Porto, Portugal
- ⁴ Institut de Biomedicina de la Universitat de Barcelona (IBUB) and Facultat de Farmàcia, Universitat de Barcelona, Av. Joan XXIII s/n, 08028 Barcelona, Spain; sruizcarmona@gmail.com
- ⁵ Programa de Investigación de Producción de Biomoléculas, Departamento de Biología Molecular y Biotecnología, Instituto de Investigaciones Biomédicas, Universidad Nacional Autónoma de México, Cd. Universitaria, Ciudad de México 04510, Mexico; adri@biomedicas.unam.mx (N.A.V.-C.); maurotru@biomedicas.unam.mx (M.T.-R.)
- ⁶ Department of Chemistry and Biochemistry, Texas Tech University, Lubbock, TX 79409, USA; joachim.weber@ttu.edu
- ⁷ Center of Medical Biotechnology, Faculty of Biology, University of Duisburg-Essen, 45127 Essen, Germany
- ⁸ Departament de Farmàcia i Tecnologia Farmacèutica, i Físicocòmica, Institut de Biomedicina (IBUB), Universitat de Barcelona, Av. Joan XXIII, 27-31, 08028 Barcelona, Spain; xbarril@ub.edu
- ⁹ Catalan Institution for Research and Advanced Studies (ICREA), 08010 Barcelona, Spain
- * Correspondence: yasser.ruizblanco@uni-due.de (Y.B.R.-B.); egarciah@unam.mx (E.G.-H.)
- † These authors contributed equally to this work.
- ‡ Current address: Cambridge Baker Systems Genomics Initiative, Baker Heart and Diabetes Institute, Melbourne, VIC 3004, Australia.



Citation: Avila-Barrientos, L.P.; Cofas-Vargas, L.F.; Agüero-Chapin, G.; Hernández-García, E.; Ruiz-Carmona, S.; Valdez-Cruz, N.A.; Trujillo-Roldán, M.; Weber, J.; Ruiz-Blanco, Y.B.; Barril, X.; et al. Computational Design of Inhibitors Targeting the Catalytic β Subunit of *Escherichia coli* F₀F₁-ATP Synthase. *Antibiotics* **2022**, *11*, 557. <https://doi.org/10.3390/antibiotics11050557>

Academic Editor: Jean-Marc Sabatier

Received: 7 March 2022

Accepted: 25 March 2022

Published: 22 April 2022

Publisher's Note: MDPI stays neutral with regard to jurisdictional claims in published maps and institutional affiliations.



Copyright: © 2022 by the authors. Licensee MDPI, Basel, Switzerland. This article is an open access article distributed under the terms and conditions of the Creative Commons Attribution (CC BY) license (<https://creativecommons.org/licenses/by/4.0/>).

Abstract: With the uncontrolled growth of multidrug-resistant bacteria, there is an urgent need to search for new therapeutic targets, to develop drugs with novel modes of bactericidal action. F₀F₁-ATP synthase plays a crucial role in bacterial bioenergetic processes, and it has emerged as an attractive antimicrobial target, validated by the pharmaceutical approval of an inhibitor to treat multidrug-resistant tuberculosis. In this work, we aimed to design, through two types of in silico strategies, new allosteric inhibitors of the ATP synthase, by targeting the catalytic β subunit, a centerpiece in communication between rotor subunits and catalytic sites, to drive the rotary mechanism. As a model system, we used the F₁ sector of *Escherichia coli*, a bacterium included in the priority list of multidrug-resistant pathogens. Drug-like molecules and an IF₁-derived peptide, designed through molecular dynamics simulations and sequence mining approaches, respectively, exhibited in vitro micromolar inhibitor potency against F₁. An analysis of bacterial and Mammalia sequences of the key structural helix-turn-turn motif of the C-terminal domain of the β subunit revealed highly and moderately conserved positions that could be exploited for the development of new species-specific allosteric inhibitors. To our knowledge, these inhibitors are the first binders computationally designed against the catalytic subunit of F₀F₁-ATP synthase.

Keywords: F₀F₁-ATP synthase; allosteric inhibition; structure-based drug design; evolutionary and PPI algorithms; peptide design

1. Introduction

At the end of the last century, there were already alarming signs of a growing health crisis because of the emergence of antimicrobial resistance (AMR) [1], which, if left unattended, would cause worldwide mass fatalities and colossal financial burden [2,3]. As it was feared, the decline in investment in the development of novel antibiotics has aggravated this crisis, reflected in the decrease in newly approved antibiotics, although a slight change in this trend was recently reported [4]. AMR microorganisms have developed effective antibiotic evasion mechanisms [5]. The need to circumvent those mechanisms prompts the search for novel pharmacological targets [4]. Bacterial bioenergetic pathways have recently unveiled a new Achilles heel to combat AMR [6], as evidenced by bedaquiline, the first approved anti-tuberculosis drug in 40 years, which targets *Mycobacterium tuberculosis* ATP synthase [7]. Furthermore, mounting evidence supports that blocking the catalytic activity of this enzyme sensitizes AMR facultative anaerobic microorganisms (*v. gr.*, *Staphylococcus aureus* and *Escherichia coli*) to the action of other antimicrobial agents [8–10]. Therefore, ATP synthase appears as a momentous pharmacological target to broaden the battlefield against the pathogens of major concern.

ATP synthase is a sophisticated molecular motor, with an efficiency of ~100% [11], made up of two functionally coupled subcomplexes: a membrane embedded proton channel, F_O , and a soluble catalytic subcomplex, F_1 . Together, F_O and F_1 harvest electrochemical gradient potential energy to produce rotational energy that is eventually converted into chemical energy as a phosphodiester bond [12,13]. The enzyme also catalyzes, with high efficiency, the hydrolysis of ATP, being able to restore the proton gradient under physiological demand (*v.gr.*, to generate membrane potential in bacteria under anaerobic conditions) [14]. The minimal architecture of this enzyme is found in bacteria (Figure 1), composed of eight types of subunits, with $F_O:ab_2c_{10-17}$ and $F_1:\alpha_3\beta_3\gamma\delta\epsilon$ stoichiometries [12,15]. Proton translocation (or sodium ions, in some species) drives the rotation of the transmembrane ring of c subunits relative to the a subunit. This rotation drives the torque of the asymmetric γ subunit, which is partially embedded in the catalytic $\alpha_3\beta_3$ ring. $\alpha_3\beta_3$ is stabilized against rotation by the stator stalk, composed of δ , b , and a subunits in bacteria [16], and by a larger number of different subunits in mitochondria [17]. ATP synthase operates under a mechanism dubbed as the binding change mechanism [18]. Each of the three catalytic sites, composed mainly of residues of the β subunit and some of the α subunit, transits through three alternating affinity states, corresponding to three different conformational states. According to the nucleotide occupancy exhibited in the first experimental F_1 structure from *Bos taurus* (Bs F_1) [19], these states are usually termed as β_E (empty binding site), β_{TP} (ATP bound), and β_{DP} (ADP bound). When the enzyme acts as a hydrolase, in an alternate progression, each β subunit goes in the order $\beta_E \rightarrow \beta_{TP} \rightarrow \beta_{DP}$, as the catalytic cycle progresses. The conformational changes in the β subunits are coupled to the formation and breakdown of contacts with the asymmetric α -helices of the γ subunit and the adjacent α subunits. In this rotary mechanism, the helix-turn-helix (HTH) motif of the β -subunit C-terminal domain (β_{Cterm}) plays a central role in the communication with the other subunits and has been described as a pushrod, pushed by the γ subunit (or which sets the γ subunit in motion in the hydrolysis direction) [20,21]. β_{Cterm} is in an open conformation in β_E , with minimal intercatenary interactions. After 120° rotation of the γ subunit, driven by ATP binding, β_{Cterm} transits into a closed conformation in β_{TP} , contacting to the γ subunit and one of the adjacent α subunits (α_{TP}). A further 120° γ -subunit rotation leads to β_{DP} , a conformation very similar to β_{TP} , except for tighter packing of its β_{Cterm} against the γ subunit and the adjacent α subunit (α_{DP}). ATP hydrolysis and ADP release occur within $0^\circ \rightarrow \sim 90^\circ$ and $\sim 90^\circ \rightarrow 120^\circ$ rotation substeps in the $\beta_{TP} \rightarrow \beta_{DP}$ and $\beta_{DP} \rightarrow \beta_E$ transitions, respectively [13]. In the self-inhibited conformation of the *Escherichia coli*'s F_1 (Ec F_1), the β subunits β_2 and β_3 exhibit β_E - and β_{TP} -like conformations, respectively, while β_1 adopts a half-closed conformation because of a steric hindrance of the C-terminal domain of the ϵ subunit in an extended conformation (Figure 1) [16,22].

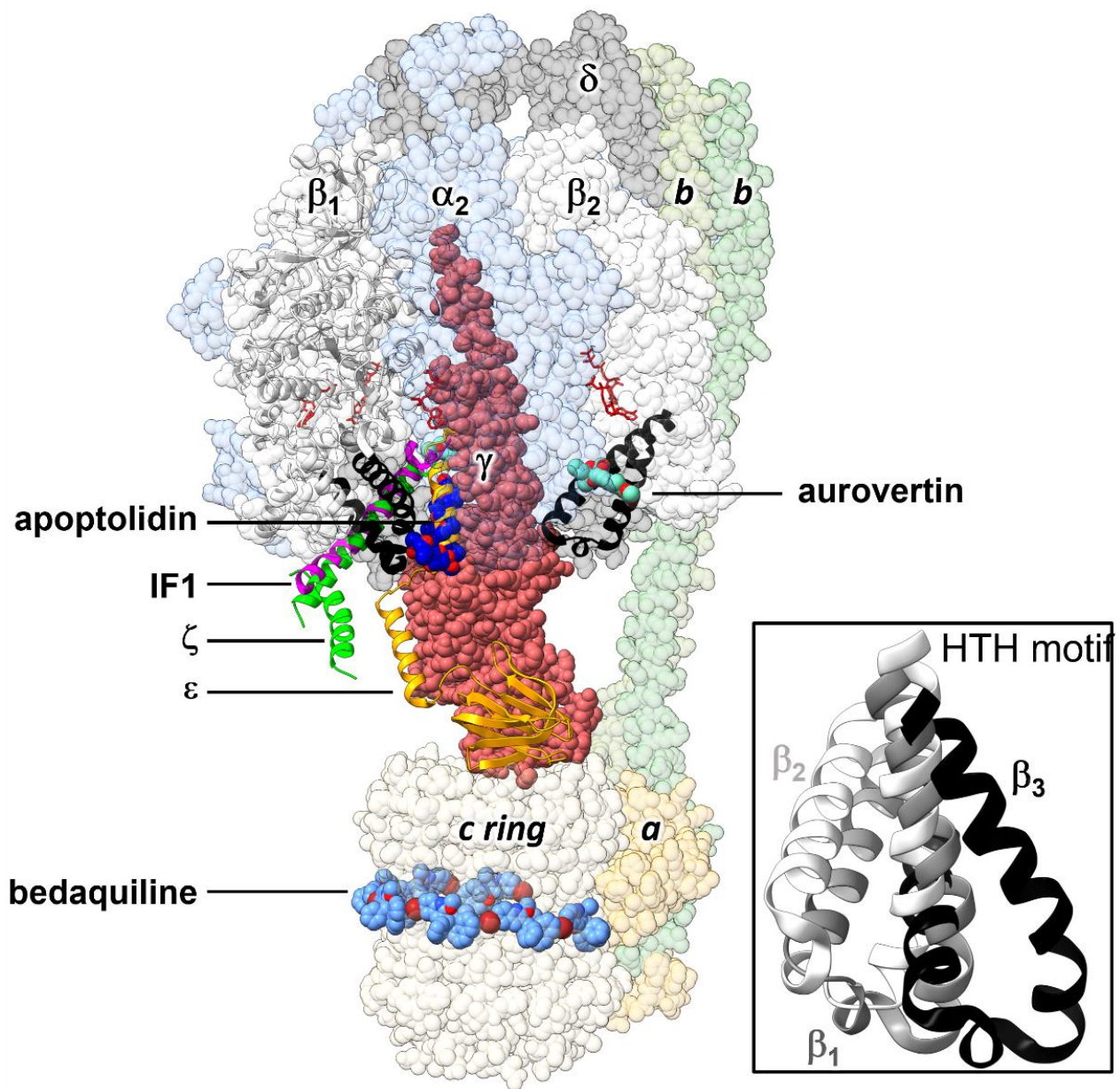


Figure 1. Schematic representation of the 3D structure of *E. coli* F₀F₁-ATP synthase, showing the binding sites of allosteric inhibitors that interact with the C-terminal domain of the β subunit. Inhibitors whose 3D structure in complex with the enzyme has been experimentally solved were docked by alignment on the cryoEM structure of the *E. coli* enzyme in an inhibited conformation by the ε subunit (PDB ID 6oqr [16]). HTH motifs of β₁ and β₂ are in black ribbons. The F₁ and F₀ subcomplexes are composed of the α₃β₃γδε and ab₂c₁₀ subunits, respectively. The endogenous inhibitory ε (PDB ID 6oqr [16]), ζ (PDB ID 5dn6 [23]) and IF1 (PDB ID 1ohh [24]) subunits are shown in ribbons. The exogenous inhibitors aurovertin B (PDB ID 1cow [25]) and the glycomacrolide apoptolidin A (PDB ID 7md3 [26]) are shown in spheres. Here, also shown is the position of the anti-tuberculosis drug bedaquiline (PDB ID 7jg8 [27]), which occupies sites equivalent to those of oligomycin in the c ring. Nucleotides are shown in sticks. **Inset:** Alignment of the HTH motifs of the three β subunits observed in the self-inhibited structure of *EcF*₁ [16,22]. In this conformation, the ε subunit hampers the closing of one β subunit, adopting a half-closed conformation (β₁). A β₁-like conformation is also observed in the complexes with the glycomacrolides apoptolidin A and ammicidin A [26].

A wealth of exogenous and endogenous ATP synthase inhibitors has been described [28,29]. Structural studies have identified several binding sites along the ATP synthase architecture for these inhibitors, revealing the existence of a diversity of allosteric mechanisms to inhibit the enzyme (Figure 1). Many of these inhibitors bind to sites involving β Cterm. The eukaryotic inhibitor IF1 [30], and the prokaryotic ϵ and ζ subunits insert an α -helix motif into a pocket formed by the $\alpha_3\beta_3$ ring and the γ subunit, near the C-terminal domains of α_{DP} and β_{DP} , thus, stopping rotational catalysis and preventing wasteful ATP consumption [31–33]. Recently, the binding site of a family of glycomacrolide inhibitors was identified, in a region involving the HTH motif of a β_1 -like subunit [26]. In addition, aurovertins, antibiotics produced by the fungus *Calcarisporium arbuscula*, target equivalent sites in the bovine β_E and β_{TP} subunits between β Cterm and the nucleotide binding domain [25]. Taken together, the existence of these non-orthosteric inhibitors indicates that β Cterm is a suitable target for the development of allosteric pharmacological modulators. Because of a less stringent evolutionary pressure, allosteric sites tend to be less conserved than catalytic sites [34–36]. This aspect is relevant to design specific ATP synthase inhibitors, since some regions of the active site of this enzyme are highly conserved across P-loop NTPases [37,38]. Furthermore, allosteric inhibitors do not compete with the substrate, so they do not require reaching an extremely high binding potency to exert an effective pharmacological action [39]. Target-based allosteric inhibitor design on ATP synthase has been limited. GaMF1 [40] and epigallocatechin gallate [41] are a notable exception. These compounds, which inhibit mycobacterial ATP synthase by binding to γ and ϵ subunits, respectively, have been obtained through pharmacophoric-restraints filtered docking studies.

Given the crucial role played by the β Cterm in driving the rotational mechanism of F_0F_1 -ATP synthase, in this work, we set out to design, through two types of in silico strategies, new allosteric inhibitors, by targeting the HTH motif of the *Escherichia coli* F_1 (Ec F_1), a bacterium included in the ESKAPEE (*Enterococcus faecium*, *Staphylococcus aureus*, *Klebsiella pneumoniae*, *Acinetobacter baumannii*, *Pseudomonas aeruginosa*, *Enterobacter spp*, and *Escherichia coli*) list of the most threatening AMR microbes [42]. The underlying idea was that the engineered binders, by interfering with the conformational transitions of this motif, will exert an allosteric effect, leading to the blocking of the enzyme's rotation. On the one hand, through a molecular dynamics (MD) simulation approach with solvent mixtures (MDmix), we identified solvent sites (SS) on the HTH motif that helped guide the high-throughput virtual screening (HTVS) of drug-like molecules [43,44]. The best hits were further filtered using the dynamic undocking method (DUck), an orthogonal technique that evaluates the work developed upon pulling the ligand out from the binding site [45]. Using a new in silico strategy, guided by evolutionary and machine learning-based methods [46], we derived peptides from IF1, based on the observation that the residues that bind this inhibitor in Bs F_1 are highly conserved in Ec F_1 . Both approaches led to the identification of drug-like and peptide hits that inhibited the hydrolytic activity of Ec F_1 with micromolar potency. Remarkably, given the different nature of the identified hits and the distinct modeling approaches, we proved the feasibility of the in silico design of ATPase inhibitors, targeting the catalytic subunit. These molecules could serve as leading scaffolds for the development of novel drugs to combat AMR bacterial strains.

2. Results

2.1. Structure-Based Design of Small Organic Inhibitors

For the design of drug-like molecules, based on the structure of ATP synthase, we performed MD simulations using the crystallographic structure of Ec F_1 , self-inhibited by the ϵ subunit and MgADP (Figure 1, PDB ID 3oaa), a distinctive conformational state of the enzyme in bacteria and chloroplasts [16,22]. In this structure, β_2 and β_3 show conformations very close to bovine β_E and β_{TP} , respectively. In contrast, β_1 adopts an intermediate conformation, since the ϵ subunit impedes the total closure of β Cterm (Figure 1 inset), a mechanism hypothesized to prevent the enzyme from falling to a low-energy state, inhibited by MgADP [47]. To sample the conformational space neighboring, the crystal

structure of EcF₁, unrestrained 20-ns simulations were performed. Judging by the time evolution of the RMSD (Figure 2A), the HTH of β₁ converged to the same conformation in all solvent and pure water replicas, except for one trajectory in ethanol, in which a slightly more open conformation of the DELSEED motif was observed (Figure 2B). The analysis of this trajectory revealed the well-defined presence ($\Delta G_{SS} \leq -1$ kcal/mol) of a solvent site cluster, in an area close to the DELSEED region and intermediate between the two HTH helices. The cluster was composed of a site for the hydroxyl's oxygen (SS_{OH}) and three sites for the methyl carbon (SS_{CT}) of ethanol (Figure 2C). The carbonyl group of G³⁷⁸ stabilized the unique SS_{OH}, while the side chains of R³⁶⁶, Y³⁶⁷, I³⁷³, V³⁸⁹, and A³⁹³ were involved in the stabilization of the SS_{CT}. Consistently, the four solvent sites were closely reproduced in three MD replicas, in which harmonic constraints ($k = 0.5$ kcal/molÅ²) were imposed on the heavy atoms of the protein to keep the HTH in open conformation (data not shown). Therefore, this open conformation of HTH, which was also significantly, albeit to a lesser degree, populated in pure water replicas, was apparently stabilized by the organic solvent.

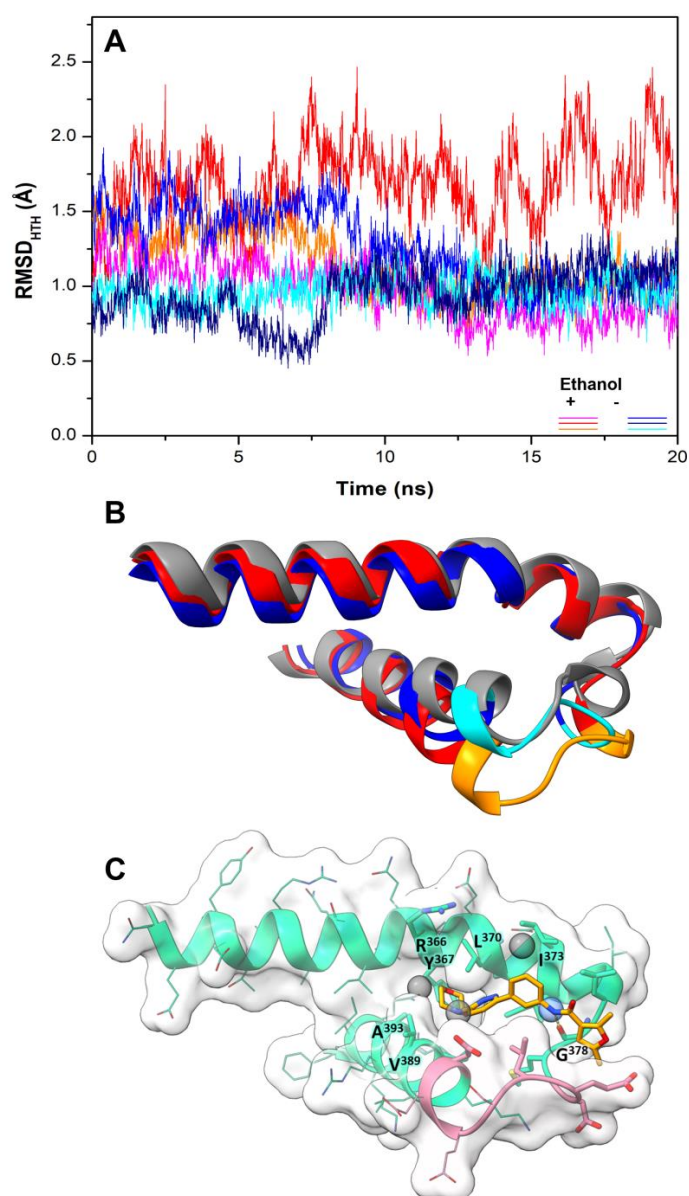
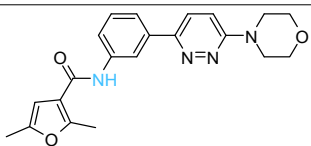
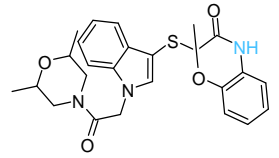
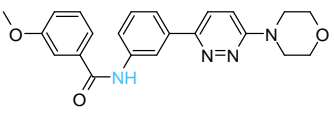
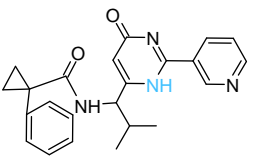
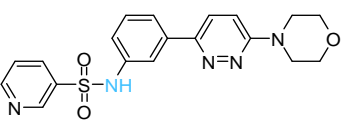


Figure 2. HTH dynamics and solvent sites determined from MD simulations. (A) RMSD was calculated using backbone atoms of the β₁ HTH motif. Values from three MD simulations in

pure water (blue colors) and three in water-ethanol mixture (red colors) are shown. **(B)** Average conformations of the HTH motif calculated over the last 10 ns of simulation. The open conformation obtained in one trajectory in a solvent mixture is shown in orange, while a closed conformation from one of the replicas in pure water is shown in blue. The DELSEED motif is in lighter color. The starting crystal conformation is in gray (PDB ID 3oaa, [22]). **(C)** Solvent sites for ethanol's methyl (gray spheres) and hydroxyl (blue sphere) groups determined from one trajectory in ethanol/water mixture. One of the ligands (Compd-5) obtained in this work by HTVS (vide infra) is shown in sticks, forming a hydrogen bond with the carbonyl group of G³⁷⁸. The DELSEED motif is in pink.

The four solvent sites observed in β_1 were used as pharmacophoric restraints to guide HTVS of $\sim 8 \times 10^6$ molecules from eight different commercial chemical libraries, using the rDock software [44]. After removing molecules with very similar chemical structures by visual inspection, the 100 top-ranked molecules, ordered according to the docking score, were additionally filtered using steering dynamics, with the DUCK method [45]. The work required (W_{QB}) to move away the hydrogen donor atom of the docked molecule to 5 Å (quasi-bound state) from the carbonyl group of G³⁷⁸ was determined, discarding those molecules with $W_{QB} < 6$ kcal/mol. As a result, 27 potential ligands were selected and purchased (Table S1). The inhibitory potency of these compounds was assayed against purified EcF₁, using the malachite green method. As shown in Table 1, five compounds displayed significant inhibition of ATPase activity at 100 μ M of inhibitor concentration. Measurements performed using the NADH-linked ATP regeneration system yielded similar inhibition values. According to the Chemaxon solubility predictor server [48], the five compounds are soluble in the micromolar range (Table 1). It is also worth mentioning that, according to the MOE software, the five hit molecules are not pan-assay interference compounds (PAINS). Only compound 18 and 26 contained a PAINS warning.

Table 1. Summary of the final active compounds designed against the HTH motif structure of EcF₁.

	Structure ^a	ΔG_{rDock} ^b (kcal/mol)	W_{QB} ^c (kcal/mol)	ΔG_{PB} ^d (kcal/mol)	Residual ATPase Activity (%) ^e	logS ^f
Compd-5		−6.0	8.7	−29	43 ± 6 (50 ± 5%)	−4.7
Compd-7		−5.5	6.0	−30	64 ± 12 (70 ± 10%)	−5.1
Compd-14		−4.5	6.7	−25	75 ± 8 (73 ± 2%)	−5.3
Compd-15		−4.3	6.0	−24	67 ± 5 (ND)	−4.9
Compd-19		−4.0	6.0	−29	77 ± 7 (70 ± 10%)	−2.8

^a NH atoms that established hydrogen bonds with the G³⁷⁸ backbone oxygen are in blue. ^b rDock score, a weighted sum of intermolecular, ligand intramolecular, site intramolecular and pharmacophoric restraints [44].

^c Work needed to separate the ligand's atom forming a hydrogen bond with the protein to a 5 Å distance, calculated with DUck [45]. ^d Molecular mechanics Poisson–Boltzmann surface area (MM-PBSA) calculated free energy [49,50]. ^e Residual ATPase activity of EcF₁ determined by the malachite method (and the ATP regenerating system, values in parentheses), incubated with 100 μM of the indicated compound, in a 50 mM Tris-SO₄ buffer solution with 1% DMSO (pH 8.0), 25 °C. Data represent the average ± standard deviation of at least 3 independent experiments. ND, not determined. ^f Predicted aqueous solubility determined with the Chemaxon solubility predictor server.

To further characterize the inhibitory effect of Compd-5, the ligand that exhibited the most potent activity, dose-response measurements were performed (Figure 3). Nonlinear analysis of the data, using the Hill equation, yielded an IC_{50} value of $62 \pm 5 \mu\text{M}$ and a Hill coefficient of 0.86 ± 0.02 , suggesting that there is no cooperativity between the three β subunits. The fitting showed a residual enzyme activity of $9 \pm 1\%$ under saturation conditions, showing that Compd-5 nearly acts as a dead-end inhibitor.

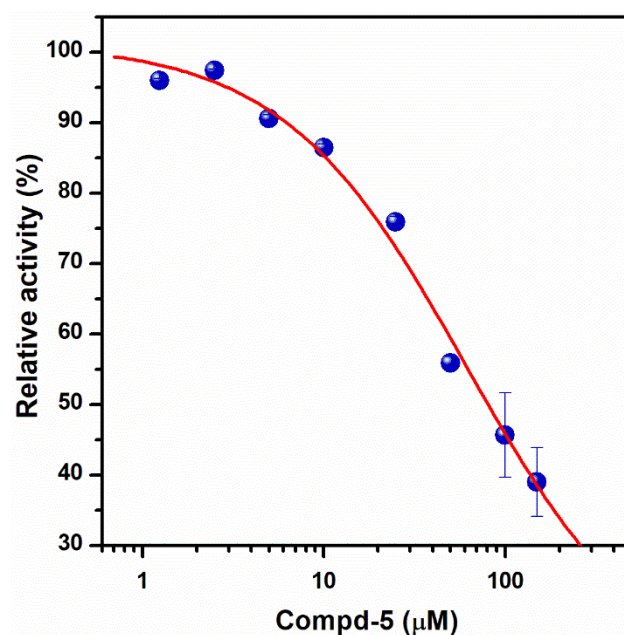


Figure 3. Dose-response plot of the inhibitory effect of Compd-5 on EcF₁. Residual ATPase activity was measured using compound concentrations in the 1.25–150 μM range, in a 100 mM Tris-SO₄ buffer solution with 1% DMSO (pH 8.0), 25 °C. The Hill equation was fitted to the experimental data, obtaining $IC_{50} = 62 \pm 5 \mu\text{M}$, $h = 0.86 \pm 0.02$, $v_r = 9 \pm 1\%$. Data shown represent the average ± standard deviation of 3 independent experiments.

All the active compounds had an NH group, serving as a hydrogen donor to the G³⁷⁸ carbonyl moiety. As an example, the predicted binding pose of Compd-5 is shown in Figure 2C. It is worth mentioning that Compd-5, Compd-14 and Compd-19 all come from the same family, being the only compounds in the tested set with the 4-(6-phenylpyridazin-3-yl)morpholine substructure (Simplified Molecular Input Line Entry System, SMILES, “[NH]c1cc(-c2nnc(N3CCOCC3)cc2)ccc1”). The binding energy (ΔG_{PB}) of the positive inhibitors was computed on the corresponding docked poses, using the molecular mechanics Poisson–Boltzmann surface area (MM-PBSA) method [49,50] and compared against the rDock scores (ΔG_{rDock}) in Table 1. Clearly, there is a better correlation of the degree of experimental inhibition with the energies calculated with rDock ($r^2 = 0.77$) than with the MM-PBSA method ($r^2 = 0.12$), which highlights the good performance of the HTVS method [43]. Finally, we computationally explored the possibility that the engineered inhibitors could also bind to the HTH motif of the other two β subunits. The pose of Compd-5 in β_1 was used to dock the ligand on the other two subunits to perform unrestrained MD simulations. Like β_1 , β_3 kept the inhibitor bound for up to 50 ns in two replicas, a suitable

time to consider the interaction as stable [51]. In contrast, the compound was consistently released from β_2 within the first nanoseconds of simulation (Figure S1).

2.2. De Novo Design of Peptide Inhibitors of EcF₁ Targeting the β Cterm

In a previous report, we introduced a de novo design method of EcF₁ peptide inhibitors [46]. The new inhibitors were designed in silico from the interfaces connecting F₀F₁-ATP synthase subunits, thus, proving the suitability of these scaffolds for the generation of a new family of inhibitors. Peptide libraries were built by applying simulated molecular evolution approaches, represented by the ROSE (random model of sequence evolution) algorithm [52], and later screened using PPI-Detect, a protein–protein interaction predictor [53], to score the binding likelihood of the peptides and EcF₁. This new in silico strategy, guided by evolutionary and machine-learning-based methods, allowed widening and exploring the relevant structural space from natural peptide fragments to generate novel protein binders [46]. Here, we leveraged this approach for the de novo design of EcF₁ peptide inhibitors, specifically targeting the β Cterm. The fourteen IF1 sequences registered in the UniProt database [54], ranging from 42 to 50 aa length, were aligned to identify conserved regions. Two conserved regions were identified in the multiple sequence alignment (MSA), resulting in two consensus regions that were considered root or parent peptides (Figure 4).

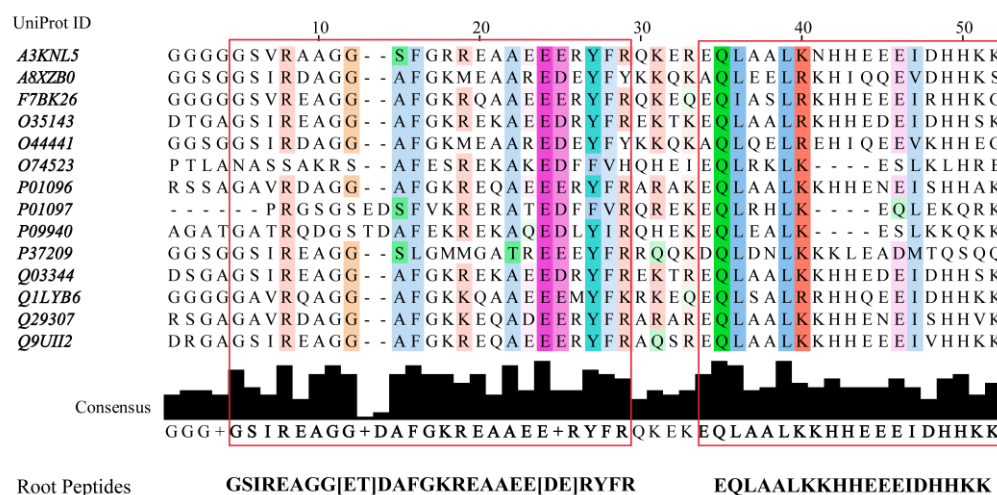


Figure 4. Multiple Sequence Alignment (MSA) performed with Multiple Alignment using Fast Fourier Transform, MAFFT, [55] for IF1 inhibitors deposited in the UniProt database. Consensus regions are identified at >40% of identity threshold at each position of the MSA. The resulting consensus regions are framed in a rectangular box. From them two root peptides were estimated IF1 sources: A3RKNL5, zebrafish. A8XZB0, Caenorhabditis briggsae. F7BK26, western clawed frog. O35143, mouse. O44441, Caenorhabditis elegans. O74523, fission yeast. P01096, bovine. P01097, baker's yeast. P09940, torula yeast. P37209, Caenorhabditis elegans. Q03344, rat. Q1LYB6, zebrafish. Q29307, pig. Q9UII2, human. Jalview ver: 2.11.1.4 was used to visualize the MSA and determine the consensus.

ROSE operates by introducing stochastic point mutations into the root amino acid sequence, which is guided by a binary phylogenetic tree and a mutability vector, representing the conservation degree of each position in the sequence. Both the root peptide and the mutability vector are obtained by multiple sequence alignment of the selected set of peptides, carried out with Multiple Alignment, using Fast Fourier Transform, MAFFT, [55] (Table S2). The obtained library was then screened using PPI-Detect, which classifies and ranks the peptides as putative binders of the targeted site [46,53]. This strategy allowed us the rational exploration of the sequence space around the selected templates. From the root peptides, 385 unique mutants were generated. These peptides have a minimum identity, relative to their root sequence, of 70%. Using PPI-Detect [53], these candidates

were screened based on their interaction likelihood with the subunit β of EcF₁ and the human sector (HsF₁). Selected candidates had to meet the following criteria: (a) Peptides with maximum interaction likelihood with HsF₁ below 0.5. (b) Peptides with maximum interaction likelihood with EcF₁ above 0.5. (c) The difference between the interaction probabilities with *E. coli* and human enzymes is at least 0.1. After applying these selection criteria, three peptides were filtered out (Table 2). Surprisingly, the selected peptides showed the highest interaction score and score difference with the central domain of the β subunit ('smart00382' domain), while a score value of ~ 0.32 was obtained for the HTH motifs of both EcF₁ and HsF₁.

Table 2. Interaction scores and chemical–physical properties of the selected peptide candidates.

Peptide	Sequence	Score ^a (EcF ₁)	Score ^a (HsF ₁)	Charge (pI) ^b	GRAVY ^b
Pept1-IF1	GSIREAGGTHAFGKRESAEEERYFR	0.512	0.402	0 (6.78)	−1.292
Pept2-IF1	GSIREAGGTDGFGKREAAEEKEYGR	0.561	0.420	−1 (5.11)	−1.392
Pept3-IF1	GSVREAGGTGAFGKRESAEEERYFR	0.580	0.479	0 (6.34)	−1.192

^a The domain 'smart00382' was mapped on the β subunits of EcF₁ and HsF₁ using the NCBI tool CD-Search [56] to identify conserved domains. The extracted fragments of the subunits were used to compute the interaction scores with the peptides. ^b Values calculated with ProtParam [57].

The negative GRAVY index evidences the polar features of these peptides and their potentially good solubility. From them, the candidate termed as Pept1-IF1 was selected for synthesis because of its neutral charge and isoelectric point value, close to 7.0. This peptide (sequence: Ac-GSIREAGGTHAFGKRESAEEERYFR-NH₂) showed inhibitory activity against EcF₁, with $IC_{50} = 155 \pm 14 \mu\text{M}$, $h = 1.1 \pm 0.1$, and $v_r = -1 \pm 3\%$ (Figure 5).

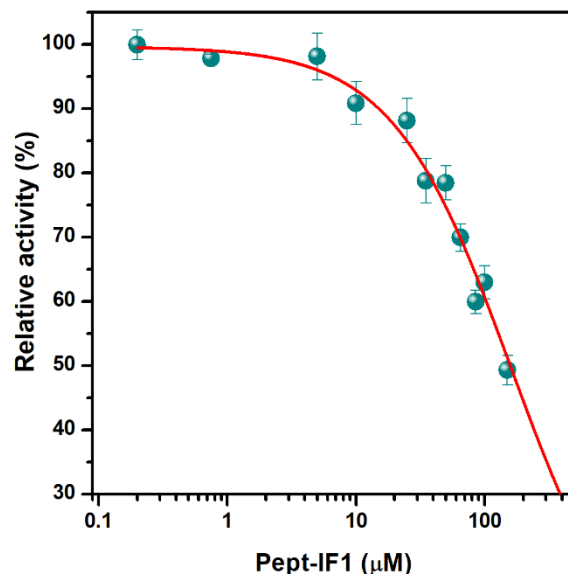


Figure 5. Dose-response plot of the inhibitory effect of Pept-IF1 on EcF₁. Residual ATPase activity was measured using peptide concentration in the 1.25–150 μM range, in a 100 mM Tris-SO₄ buffer solution with 1% DMSO (pH 8.0), 25 °C. The Hill equation was fitted to the experimental data, obtaining $IC_{50} = 155 \pm 14 \mu\text{M}$, $h = 1.1 \pm 0.1$, $v_r = -1 \pm 3\%$. Data represent the average \pm standard deviation of 3 independent experiments.

2.3. Sequence Conservation of the HTH Motif in Bacteria

Given the observed inhibition results and the functional relevance of the HTH motif, we set out to explore the sequence conservation of this motif in bacterial species. From the UniProt database, 23,125 b-subunit sequences, from all bacterial F₀F₁-ATP synthases, were retrieved [54]. The dataset was aligned to generate sequence logos of the HTH

motif [58,59]. As previously observed in less comprehensive sequence analysis [60,61], the HTH motif is significantly conserved among bacteria (Figure 6), and even more conserved among Mammalia (Figure S2). The HTH motif comprises the α -helix 1 (H1: R³⁵¹-I³⁷⁶), the turn (T: L³⁷⁷-S³⁸³), and the α -helix 2 (H2: E³⁸⁴-R³⁹⁹) segments (*E. coli* numbering). The ³⁸⁰DELSEED³⁸⁶ motif is within the C-terminal and N-terminal regions of T and H2, respectively. The most conserved regions encompass the central region D³⁷⁰-K³⁸⁷ (or HTH tip, which besides the DELSEED, also includes the largely conserved ³⁷²DIILG³⁷⁸ segment), the C-terminal segment ³⁹²RARKI³⁹⁶, plus some scattered, mostly hydrophobic residues, in H1 and H2. An analysis of the experimental 3D structures of F₁ reveals that, with few exceptions, the most conserved residues in the HTH motif also form interactions with highly conserved residues, located either in the same subunit (mostly in the HTH motif itself) or in the adjacent α , β , or γ subunits (Figure S3). Further, 18 out of 45 residues of the HTH motif show significant variability. The most variable segment is in H1, while the most conserved is in T. Importantly, the binding site of the compounds, designed herein, includes portions of the conserved DIILG and DELSEED segments, as well as some moderately conserved residues. In particular, the Bacilli class shows the most contrasting differences regarding the human enzyme (Figure S4), a characteristic that could be exploitable to optimize molecules capable of selectively recognizing pathogens of this taxonomic group, and that do not bind to the human enzyme.

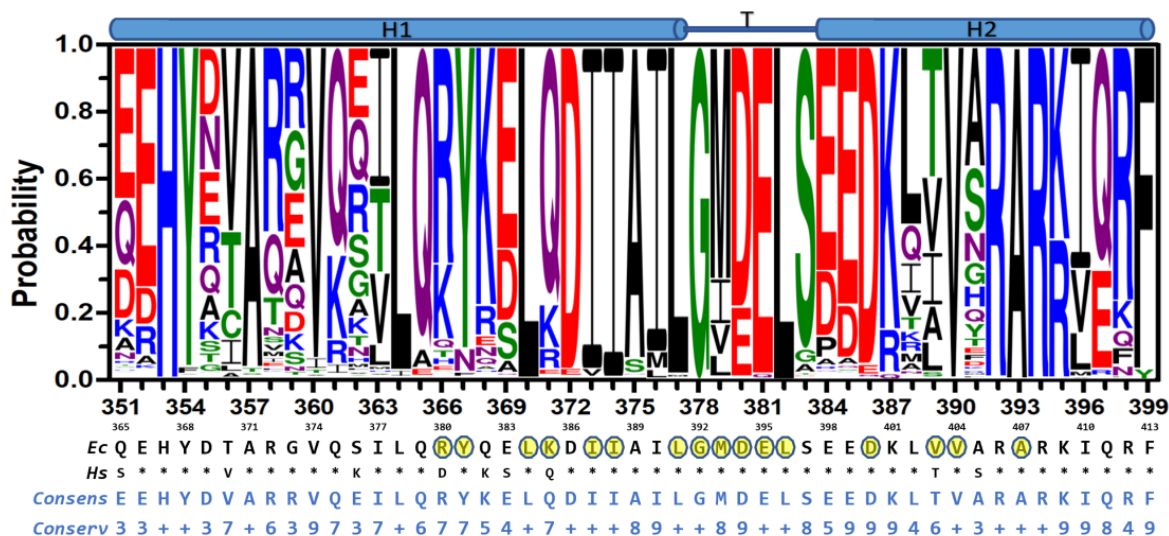


Figure 6. Conservation of the HTH motif in bacteria. Residue numbering in the up and down rows corresponds to the *E. coli* and human sequences, respectively. Multiple sequence alignment of 23,125 entries was performed with Clustal Omega [59]. Logos were generated using the Weblogo3 server [58]. Consensus, *E. coli* (*Ec*) and human (*Hs*) sequences are shown in the x-axis for comparison. Human residues identical to *E. coli* residues are shown with asterisks. The *Conserv* row corresponds to a conservation scale ranging from 0 (null conservation) to 10 (= +, complete conservation of physicochemical properties of the amino acid group) as defined in [62]. Residues within 5 Å of Compd-5 are highlighted in yellow.

3. Discussion

Although the declining trend of newly approved antibiotics has recently reversed, infections caused by AMR bacteria are still an alarming threat to global public health [4]. Interfering bioenergetic pathways is an emerging strategy to combat pathogens [6]. Indeed, pharmacological-approved bedaquiline has attested that ATP synthase inhibition can be successfully harnessed to target aerobic organisms, such as *M. tuberculosis* [63]. In addition, AMR facultative anaerobes, including the ESKAPEE pathogens *S. aureus* and *E. coli*, lose resistance towards antibiotics upon ATP synthase inhibition [64,65]. Given the major role played by β Cterm in inter-subunit communication, orchestrating the rotary mechanism

of ATP synthase, we strived to design molecules capable of selectively targeting the HTH motif. Inspired by the effect that endogenous regulatory subunits [66–68], and some peptide venoms [69] and other exogenous inhibitors [26] have on the F₁ subcomplex, the underlying idea was that by interfering with the conformational changes that the HTH motif undergoes, an inhibitory effect on the enzymatic activity can be achieved. To do this, we used two widely different *in silico* design strategies, one based on target 3D structure [70] and the other on peptide sequence data mining [46], obtaining organic molecules and an IF1-derived peptide, whose inhibitory potencies against EcF₁ were in the micromolar range, comparable to those of known natural inhibitors, such as polyphenols and venom peptides, among others [28,29,71].

It has been shown, for an increasing number of proteins, that solvent site clusters map both orthosteric and allosteric sites [43,72]. Thus, besides identifying critical interaction points with substrates or natural ligands, MDmix-determined solvent sites have proved valuable as pharmacophoric restraints in HTVS [44,73], improving the rate of true-positive hits and the discovery of new kinds of inhibitors and binding probes [74,75]. Furthermore, by relying exclusively on the interactions determined by the force field and the kinetic energy of the atoms in the system, MDmix unbiasedly maps entire protein surfaces, opening a window of opportunity to identify potential allosteric sites that may be difficult to detect experimentally or by knowledge-based potential methods [76,77]. In this work, MD-determined solvent sites were used to guide the docking of drug-like molecules on the HTH motif. The best-ranked hits obtained from our HTVS were further filtered by steering MD, a technique that has been used to develop new kinds of inhibitors against HSP90 [45] and several oncogenic tyrosine-kinases [78]. The combined use of these orthogonal approaches that evaluate equilibrium- and trajectory-derived energies, respectively, allowed us to identify and experimentally validate novel inhibitors of EcF₁.

The five inhibitory compounds (Table 1) showed a nitrogen atom that hydrogen bonded to, the carbonyl oxygen of the completely conserved G³⁷⁸ at the beginning of the HTH turn. In addition, hydrophobic contacts were established with H1 and H2 residues. Taken together, Compd-5, Compd-14 and Compd-19, the three 4-(6-phenylpyridazin-3-yl)morpholine-containing compounds, suggest the amide/sulfonamide position is amenable to a broad range of substituents and could be used to increase potency and modulate physicochemical properties. It is worth mentioning that Compd-5, our most potent inhibitor, is a relatively small molecule (MW = 378.2 Da), providing the opportunity to add chemical groups to it, to obtain more potent molecules. To our knowledge, no other activity for this compound has been reported so far [79]. Compd-7, our second-best inhibitor, with an overall different chemical structure, has a dimethylmorpholine moiety and, like Compd-14, a methoxyphenyl group. Compd-19 has no morpholine moiety, and the nitrogen with which it would hydrogen bond to, G³⁷⁸, is within a hydroxypyrimidine. To our knowledge, these are the first reported inhibitors designed to bind to a site formed within the HTH motif of the ATP-synthase β subunit.

In a previous report, we introduced a *de novo* design method of EcF₁ peptide inhibitors [46]. The new inhibitors were designed *in silico* from the interfaces connecting F_OF₁-ATP synthase subunits, through a combination of simulated molecular evolution [52] and protein–protein interaction prediction [53] algorithms. The *in vitro* inhibitory capacity of the designed peptides proved the suitability of these scaffolds and the strategy for the generation of new inhibitor families. In this work, we derived new peptide sequences from known IF1 sequences. In contrast to the root IF1 peptides, which are incapable of inhibition of bacterial F₁ ATPase [24,80], Pept-IF1 inhibited EcF₁ with micromolar potency. However, to verify whether Pept-IF1 exhibits species discrimination and to determine its actual binding site on the β subunit, further experimental characterization is needed.

Antibiotics require tuned selectivity to achieve reliable discrimination between the pathogen target and the human or animal ortholog. Bedaquiline was initially proposed as a specific antibiotic for some species of the *Mycobacterium* genus. However, recent evidence has shown that the human enzyme is also susceptible to this antibiotic [81]. In addition, the

c subunit, the binding target of bedaquiline, shows a low conservation among bacterial ATP synthases (e.g., mean identity of 33 ± 9 vs. $62 \pm 8\%$ of β subunits). Thus, unsurprisingly, bacteria can also evade this antibiotic, through mutations in the *c*-subunit-encoding *uncE* gene [82]. In contrast to the bedaquiline-binding site (mean identity $39 \pm 20\%$ in all bacteria), the HTH motif encompasses highly conserved sequence segments intercalated with variable positions (mean identity $69 \pm 10\%$ among bacteria). Furthermore, many of the HTH-conserved residues establish inter/intracatenary contacts with other highly conserved residues (Figure S3). Therefore, the HTH motif may offer a suitable target for allosteric drug discovery [83], as recently epitomized by the design of allosteric inhibitors against bacterial and viral enzymes, using conserved residues as binding anchors [84,85].

Site-directed mutagenic studies have unveiled that the rotary mechanism withstands severe changes in the HTH sequence [20,61,86–92]. Indeed, this rotational robustness is rooted in the fact that the γ -less $\alpha_3\beta_3$ subcomplex, although in a largely decreased way, exhibits catalysis and alternating conformational changes [93], while isolated α and β subunits also undergo nucleotide-induced rearrangements that resemble those observed in the F_1 subcomplex [21,94]. *Bacillus* PS3 enzymes, with deletions of up to 9 or 13 residues in HTH, keep catalytic activity in the synthesis or hydrolysis direction, respectively [20,61,90]. These results, together with point mutations in the HTH tip, led to the proposal that “... the physical length, rather than residue-specific interactions, of helix-1 is important for torque generation” [20], while the high conservation of some residues is due to the interaction that they establish with the regulatory subunits of the enzyme [88]. However, it has been repeatedly observed that *in vitro* mutations of the HTH sequence led to modifications of highly variable magnitude in the catalytic activity of the enzyme. The effects of these perturbations on oxidative phosphorylation and other ATP synthase-coupled processes on metabolic homeostasis have been scarcely studied [95,96]. Although it remains to be validated whether the inhibition of ATP synthase through molecules that bind the HTH motif is a feasible route for the development of new antibiotics, the most relevant finding of our study is the possibility of computationally predicting and validating novel sites of allosteric modulation, as biological evolution has repeatedly proved, with multiple sites for endogenous and exogenous inhibitors of this enzyme. This opens the door to the search for new pharmacological strategies, not only to attack infectious agents, but also to develop ATP synthase pharmacological modulators in metabolic and cellular contexts, where this enzyme plays a relevant role in the progression and establishment of pathologies [97,98].

4. Materials and Methods

4.1. Molecular Dynamics Simulations

MD trajectories were performed with the AMBER 14 suite using the FF99SB force field [99]. All simulations were carried out using the crystal structure of EcF₁ (PDB ID 3oaa [22]). Modeling of protein missing atoms, N- and C-termini capping, and protonation at pH 7.4 were carried out with the Molecular Operating Environment (MOE, [100]). Using AMBER's tLeap, the protein was placed in a truncated octahedral box spanning 18.0 Å further from the solute in each direction and solvated using a pre-equilibrated box of solvent containing pure water or 20% *v/v* ethanol/water. TIP3P water model was used. The system was first geometrically optimized (5000 cycles) to adjust the solvent orientation and eliminate local clashes, using the steepest descent algorithm. Initial velocities were assigned to get a 150 K distribution. The temperature was slowly raised to 300 K in 0.8 ns keeping the volume constant. The system was further equilibrated for one ns at 300 K in the NPT ensemble. The production was run in the NPT ensemble, using periodic boundary conditions. Temperature and pressure control were achieved using the Langevin thermostat and Berendsen barostat, respectively. Long-range electrostatic interactions were accounted for using the particle-mesh Ewald summation method as implemented in the PMEMD module of the AMBER suite, with a cut-off value of 9.0 Å to split direct electrostatics and Ewald summation [101,102]. The SHAKE algorithm was enabled and the integration timestep was 2fs. Running scripts were set up with the help of the pyMDMix

software [43,103]. Trajectory analysis was performed with CPPTRAJ [104] and Chimera UCSF v14.1 [105]. Trajectories were run in triplicate. All the structure drawings were generated with ChimeraX [106].

4.2. Identification of Solvent Sites, Guided Docking, and Dynamic Undocking

Solvent sites were determined using the MDmix method as described elsewhere [43]. After trajectories were aligned, density maps for probe atoms were obtained by building a static mesh of grids over the entire simulation box and counting appearance of probe atoms in each grid during the trajectory. The observed appearance was converted into binding free energy (ΔG_{SS}) applying the Boltzmann relationship, considering the observed probe atom distribution with an expected distribution in bulk solvent at 1.0 M. Solvent sites were filtered imposing an energy threshold of -1 kcal/mol. Compound libraries from Specs, Asinex, Enamine, Vitas M, ChemBridge, Key Organics, Princeton Biomolecular Research, and Life Chemicals, with a total of $\sim 8 \times 10^6$ molecules, were docked using rDock [44]. Solvent sites were used as pharmacophores to filter compound libraries. A penalty score that increased proportionally to the square of the distance to the required solvent sites was applied when the distance was larger than 2 Å. Best ranked ligands were further filtered using steered molecular dynamics (SMD) simulations using the dynamic undocking method DUck as described elsewhere [45]. A total of 100 SMD simulations yielding 50 ns per ligand were run, imposing harmonic restraints with a force constant of 1.0 kcal/molÅ² on all receptor non-hydrogen atoms to preserve the protein conformation. Compounds were filtered out according to the work (ΔG_{QB}) needed to separate the ligand's atom forming a hydrogen bond with the β -subunit G³⁷⁸ carbonyl oxygen to a 5.0 Å distance, using a cutoff value of 6.0 kcal/mol. A workflow illustrating the process from the identification of solvent sites to dynamic undocking has been published elsewhere [78].

4.3. Engineering Peptide Inhibitors via Evolutionary and Protein–Protein Interaction Algorithms

IF1-based peptide inhibitors were derived as recently described elsewhere [46]. IF1 sequences retrieved from the UniProt database [54] were used to estimate consensus sequences that served as the root peptide to generate offspring candidates (peptide library) by applying simulated molecular evolution approaches, represented by the ROSE (random model of sequence evolution) algorithm [52] (Figure 7). The structural diversity generated by ROSE is guided by evolutionary parameters, which were tuned to develop a diversity-oriented sampling around the root sequence. The library was subsequently screened using PPI-Detect, a protein–protein interaction predictor [53,107], to score the binding likelihood of the peptides and EcF₁.

4.4. Protein Production and Purification

Unless stated otherwise, all the chemicals were from FORMEDIUM (Norfolk, UK). EcF₁ was recombinantly expressed in *E. coli* strain DK8 using the pBWU13.4 plasmid containing the *unc* operon [108]. Briefly, *E. coli* membranes carrying EcF₁ were first washed in the presence of protease inhibitors 6-aminohexanoic acid and p-aminobenzamidine, and finally in the presence of the former to solubilize the enzyme. The subcomplex was then purified by ion exchange and size exclusion chromatography using Whatman DE52 Cellulose and Sephacryl S-300 resin columns. Protein concentrations were determined using the Pierce BCA Protein Assay Kit (Thermo-Fisher, Waltham, MA, USA).

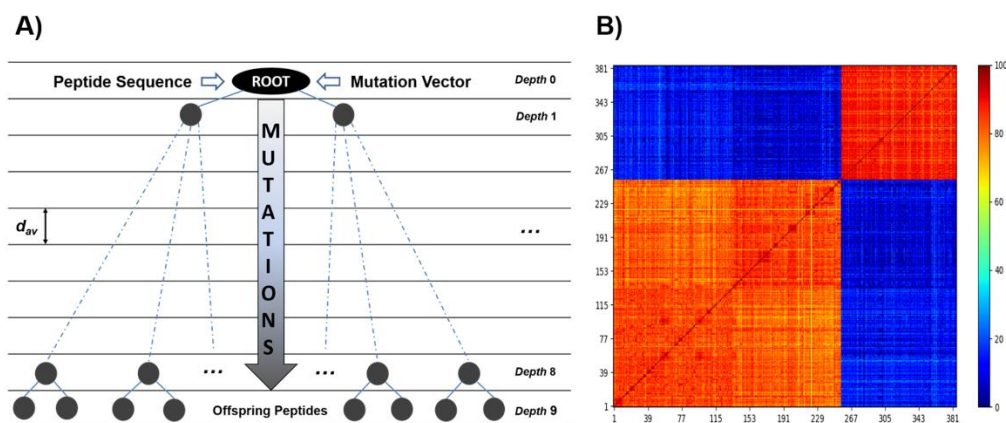


Figure 7. In silico design of a diversity-oriented peptide library. (A) Workflow illustrating the application of ROSE algorithm (<https://bibiserv.cebitec.uni-bielefeld.de/rose>, accessed on 12 March 2019). Root peptides and their corresponding mutation vectors are the input data. Besides the mutation vectors, ROSE also uses a binary tree to guide the stochastic point mutations on the root peptides. The binary tree topology is determined by the number of nodes (1023), depth (9) and average distance (d_{av} = 5–20 PAMs). ROSE was calibrated to keep a minimum identity of ~70% of the generated peptides with the corresponding root sequence. The obtained library was composed of 385 unique peptides. (B) Heatmap showing the identity matrix among the generated peptides. Two blocks are distinguished, which corresponds to the root peptides selected from different fragments of IF1.

4.5. ATPase Activity Assays

The malachite green assay was used to determine ATPase activities as previously described [109]. All compounds were assayed in a concentration range spanning 0.05–150 μ M, incubated with 10 nM (0.5 pmol) *EcF*₁ (50 mM Tris- SO_4 pH 8.0, 1% DMSO) for 1 h at 30 °C in a total volume of 30 μ L in 96-well microplates. Reactions were started by adding 20 μ L 1 mM MgATP, incubated at 25 °C for 2 min and then stopped with 200 μ L of 3.28 M H_2SO_4 and 15 mM $(\text{NH}_4)\text{Mo}_7\text{O}_{24}$ solution. Absorbance was read at 610 nm using a microplate reader (Biotek). The ATP regenerating system [110] was also used to determine ATPase activities. Experiments were carried out in a 50 mM KCl, 3 mM MgCl_2 , 1.5 mM phosphoenolpyruvate, 300 mM NADH, 50 mM Tris pH 8.0, buffered solution incubating 3 U of rabbit pyruvate kinase (Merck Inc., Kenilworth, NJ, USA), 4.2 U of rabbit lactic dehydrogenase (Merck Inc.), 5.2 nM *EcF*₁ with 100 μ M of assayed compounds, for 1 h at 30 °C in 120 μ L per well in 96-well microplates. Reactions were started by adding 30 μ L of a 50 mM KCl, 3 mM MgCl_2 , 1.5 mM phosphoenolpyruvate, 300 mM NADH, 50 mM Tris pH 8.0 solution, including 1 mM ATP. ATPase activity was monitored through absorbance changes at 340 nm for 2 min in a microplate reader (Biotek, Winooski, VT, USA).

The concentration of inhibitor required to achieve a 50% reduction in enzymatic activity, IC_{50} , was obtained using the Hill equation:

$$\frac{v_i}{v_0} = \frac{[Inh]^h}{IC_{50}^h + [Inh]^h} + v_r$$

where v_0 and v_i are the initial catalytic velocities in absence and in presence of a given concentration of the inhibitor molecule, $[Inh]$, h is the Hill coefficient and v_r is the residual velocity under saturation conditions by the inhibitor.

4.6. Sequence Analysis of the HTH Motif

ATP synthase b subunits sequences from bacteria and Mammalia taxa were retrieved from the UniProt database [54]. Jalview2 [111] was used to curate the database, excluding redundant sequences (identity < 100%), yielding 23,125 and 142 sequences for bacteria and

Mammalia groups, respectively. The curated database was used to generate a multiple sequence alignment with Clustal Omega [59]. Sequence logos of the HTH motif were generated using the Weblogo3 server [58]. Very similar logo results were obtained for both taxonomic groups using a redundancy sequence identity cutoff of <98% or <99%.

Supplementary Materials: The following supporting information can be downloaded at: <https://www.mdpi.com/article/10.3390/antibiotics11050557/s1>, Table S1: Docked organic molecules on the HTH with best scores according to rDock and DUck methods; Table S2: Root peptides and mutation vectors for each peptide inhibitor family (IF1 and Heterogeneous Set); Figure S1: Distance between the carbonyl oxygen of G378 and the amino nitrogen of Compd-5 as a function of time. Figure S2: Conservation of the HTH motif in Mammalia class. Figure S3: Conserved contacts between residues of the HTH motif and neighboring subunits [112]. Figure S4: Conservation of the HTH motif in Bacilli class. [58,59,62,112] are cited in Supplementary Materials.

Author Contributions: Conceptualization, E.G.-H. and Y.B.R.-B.; methodology, X.B., S.R.-C., E.H.-G., N.A.V.-C., M.T.-R. and J.W.; formal analysis, L.P.A.-B., L.F.C.-V., G.A.-C., Y.B.R.-B. and E.G.-H.; investigation, L.P.A.-B. and L.F.C.-V.; writing—original draft preparation, L.P.A.-B., L.F.C.-V., G.A.-C., Y.B.R.-B. and E.G.-H.; writing—review and editing, all authors; funding acquisition, E.G.-H. and G.A.-C. All authors have read and agreed to the published version of the manuscript.

Funding: Luis Pablo Avila-Barrientos and Luis Fernando Cofas-Vargas are students from Programa de Doctorado en Ciencias Bioquímicas, Universidad Nacional Autónoma de México (UNAM), and received fellowships No. 275485 and 508395, respectively, from CONACyT, México. This work was financed, in part, by DGAPA, UNAM [PAPIIT IN206221]. G.A.-C. was supported by national funds through FCT—Foundation for Science and Technology—within the scope of UIDB/04423/2020 and UIDP/04423/2020. We would like to thank Programa de Apoyo a los Estudios de Posgrado (PAEP) from Universidad Nacional Autónoma de México for the stipend awarded to LPAB for a research stay at Texas Tech University under guidance of JW.

Institutional Review Board Statement: Not applicable.

Informed Consent Statement: Not applicable.

Data Availability Statement: Not applicable.

Conflicts of Interest: The authors declare no conflict of interest. The funders had no role in the design of the study; in the collection, analyses, or interpretation of data; in the writing of the manuscript, or in the decision to publish the results.

References

1. Casadevall, A. Crisis in infectious diseases: 2 decades later. *Clin. Infect. Dis.* **2017**, *64*, 823–828. [CrossRef]
2. Taylor, J.; Hafner, M.; Yerushalmi, E.; Smith, R.; Bellasio, J.; Vardavas, R.; Bienkowska-gibbs, T.; Rubin, J. *Estimating the Economic Costs of Antimicrobial Resistance: Model and Results*; RAND Corporation: Cambridge, UK, 2014.
3. Review on Antimicrobial Resistance (London), & Grande-Bretagne. Antimicrobial Resistance: Tackling a Crisis for the Health and Wealth of Nations: December 2014. Available online: <https://www.naturallivestockfarming.com/wp-content/uploads/2015/09/Antibiotics-UK-dec-2014-Review-paper-on-health-wealth1.pdf> (accessed on 6 March 2022).
4. Talbot, G.H.; Jezek, A.; Murray, B.E.; Jones, R.N.; Ebright, R.H.; Nau, G.J.; Rodvold, K.A.; Newland, J.G.; Boucher, H.W. Infectious Diseases Society of America The Infectious Diseases Society of America's 10 × '20 Initiative (10 New Systemic Antibacterial Agents US Food and Drug Administration Approved by 2020): Is 20 × '20 a Possibility? *Clin. Infect. Dis.* **2019**, *69*, 1–11. [CrossRef]
5. Varela, M.F.; Stephen, J.; Lekshmi, M.; Ojha, M.; Wenzel, N.; Sanford, L.M.; Hernandez, A.J.; Parvathi, A.; Kumar, S.H. Bacterial resistance to antimicrobial agents. *Antibiotics* **2021**, *10*, 593. [CrossRef]
6. Hards, K.; Cook, G.M. Targeting bacterial energetics to produce new antimicrobials. *Drug Resist. Updat.* **2018**, *36*, 1–12. [CrossRef]
7. Diacon, A.; Pym, A.; Grobusch, M.; Patientia, R.; Rustumjee, R.; Page-Shipp, L.; Pistorius, C.; Krause, R.; Bogoshi, M.; Churchyard, G.; et al. The diarylquinoline TMC207 for Multidrug-Resistant Tuberculosis. *N. Engl. J. Med.* **2009**, *360*, 2397–2405. [CrossRef]
8. Vestergaard, M.; Nøhr-Meldgaard, K.; Bojer, M.S.; Krogsgård Nielsen, C.; Meyer, R.L.; Slavetinsky, C.; Peschel, A.; Ingmer, H. Inhibition of the ATP Synthase Eliminates the Intrinsic Resistance of Staphylococcus aureus towards Polymyxins. *MBio* **2017**, *8*, e01114–e01117. [CrossRef]
9. Liu, L.; Beck, C.; Nøhr-Meldgaard, K.; Peschel, A.; Kretschmer, D.; Ingmer, H.; Vestergaard, M. Inhibition of the ATP synthase sensitizes Staphylococcus aureus towards human antimicrobial peptides. *Sci. Rep.* **2020**, *10*, 11391. [CrossRef]

10. Liu, A.; Tran, L.; Becket, E.; Lee, K.; Chinn, L.; Park, E.; Tran, K.; Miller, J.H. Antibiotic Sensitivity Profiles Determined with an Escherichia coli Gene Knockout Collection: Generating an Antibiotic Bar Code. *Antimicrob. Agents Chemother.* **2010**, *54*, 1393–1403. [[CrossRef](#)]
11. Kinoshita, K.; Yasuda, R.; Noji, H.; Adachi, K. A rotary molecular motor that can work at near 100% efficiency. *Philos. Trans. R. Soc. London. Ser. B Biol. Sci.* **2000**, *355*, 473–489. [[CrossRef](#)]
12. Kühlbrandt, W. Structure and Mechanisms of F-Type ATP Synthases. *Annu. Rev. Biochem.* **2019**, *88*, 515–549. [[CrossRef](#)] [[PubMed](#)]
13. Murphy, B.J.; Klusch, N.; Langer, J.; Mills, D.J.; Yildiz, Ö.; Kühlbrandt, W. Rotary substates of mitochondrial ATP synthase reveal the basis of flexible F1-Fo coupling. *Science* **2019**, *364*, eaaw9128. [[CrossRef](#)] [[PubMed](#)]
14. Rees, D.M.; Montgomery, M.G.; Leslie, A.G.W.; Walker, J.E. Structural evidence of a new catalytic intermediate in the pathway of ATP hydrolysis by F1-ATPase from bovine heart mitochondria. *Proc. Natl. Acad. Sci. USA* **2012**, *109*, 11139–11143. [[CrossRef](#)] [[PubMed](#)]
15. Schulz, S.; Wilkes, M.; Mills, D.J.; Kühlbrandt, W.; Meier, T. Molecular architecture of the N-type ATPase rotor ring from *Burkholderia pseudomallei*. *EMBO Rep.* **2017**, *18*, 526–535. [[CrossRef](#)] [[PubMed](#)]
16. Sobti, M.; Walshe, J.L.; Wu, D.; Ishmukhametov, R.; Zeng, Y.C.; Robinson, C.V.; Berry, R.M.; Stewart, A.G. Cryo-EM structures provide insight into how E. coli F1Fo ATP synthase accommodates symmetry mismatch. *Nat. Commun.* **2020**, *11*, 2615. [[CrossRef](#)]
17. Gu, J.; Zhang, L.; Zong, S.; Guo, R.; Liu, T.; Yi, J.; Wang, P.; Zhuo, W.; Yang, M. Cryo-EM structure of the mammalian ATP synthase tetramer bound with inhibitory protein IF1. *Science* **2019**, *364*, 1068–1075. [[CrossRef](#)]
18. Boyer, P.D. The binding change mechanism for ATP synthase—Some probabilities and possibilities. *BBA—Bioenerg.* **1993**, *1140*, 215–250. [[CrossRef](#)]
19. Abrahams, J.P.; Leslie, A.G.W.; Lutter, R.; Walker, J.E. Structure at 2.8 Å resolution of F1-ATPase from bovine heart-mitochondria. *Nature* **1994**, *370*, 621–628. [[CrossRef](#)]
20. Usukura, E.; Suzuki, T.; Furuike, S.; Soga, N.; Saita, E.-I.; Hisabori, T.; Kinoshita, K.; Yoshida, M.; Yoshida, M. Torque generation and utilization in motor enzyme F0F1-ATP synthase: Half-torque F1 with short-sized pushrod helix and reduced ATP Synthesis by half-torque F0F1. *J. Biol. Chem.* **2012**, *287*, 1884–1891. [[CrossRef](#)]
21. Pulido, N.O.; Salcedo, G.; Pérez-Hernández, G.; José-Núñez, C.; Velázquez-Campoy, A.; García-Hernández, E. Energetic effects of magnesium in the recognition of adenosine nucleotides by the F1-ATPase β subunit. *Biochemistry* **2010**, *49*, 5258–5268. [[CrossRef](#)] [[PubMed](#)]
22. Cingolani, G.; Duncan, T.M. Structure of the ATP synthase catalytic complex (F1) from Escherichia coli in an autoinhibited conformation. *Nat. Struct. Mol. Biol.* **2011**, *18*, 701–707. [[CrossRef](#)]
23. Morales-Rios, E.; Montgomery, M.G.; Leslie, A.G.W.; Walker, J.E. Structure of ATP synthase from *Paracoccus denitrificans* determined by X-ray crystallography at 4.0 Å resolution. *Proc. Natl. Acad. Sci. USA* **2015**, *112*, 13231–13236. [[CrossRef](#)] [[PubMed](#)]
24. Cabezón, E.; Montgomery, M.G.; Leslie, A.G.W.; Walker, J.E. The structure of bovine F1-ATPase in complex with its regulatory protein IF1. *Nat. Struct. Biol.* **2003**, *10*, 744–750. [[CrossRef](#)] [[PubMed](#)]
25. Van Raaij, M.J.; Abrahams, J.P.; Leslie, A.G.W.; Walker, J.E. The structure of bovine F1-ATPase complexed with the antibiotic inhibitor aurovertin B. *Proc. Natl. Acad. Sci. USA* **1996**, *93*, 6913–6917. [[CrossRef](#)] [[PubMed](#)]
26. Reisman, B.J.; Guo, H.; Ramsey, H.E.; Wright, M.T.; Reinfeld, B.I.; Ferrell, P.B.; Sulikowski, G.A.; Rathmell, W.K.; Savona, M.R.; Plate, L.; et al. Apoptolidin family glycomacrolides target leukemia through inhibition of ATP synthase. *Nat. Chem. Biol.* **2021**, *11*, 909. [[CrossRef](#)] [[PubMed](#)]
27. Guo, H.; Courbon, G.M.; Bueller, S.A.; Mai, J.; Liu, J.; Rubinstein, J.L. Structure of mycobacterial ATP synthase bound to the tuberculosis drug bedaquiline. *Nature* **2021**, *589*, 143–147. [[CrossRef](#)] [[PubMed](#)]
28. Hong, S.; Pedersen, P.L. ATP synthase and the actions of inhibitors utilized to study its roles in human health, disease, and other scientific areas. *Microbiol. Mol. Biol. Rev.* **2008**, *72*, 590–641, Table of Contents. [[CrossRef](#)]
29. Patel, B.A.; D’Amico, T.L.; Blagg, B.S.J. Natural products and other inhibitors of F1FO ATP synthase. *Eur. J. Med. Chem.* **2020**, *207*, 112779. [[CrossRef](#)]
30. Gledhill, J.R.; Walker, J.E. Inhibition sites in F1-ATPase from bovine heart mitochondria. *Biochem. J.* **2005**, *386*, 591–598. [[CrossRef](#)]
31. Feniouk, B.A.; Suzuki, T.; Yoshida, M. The role of subunit epsilon in the catalysis and regulation of F0F1-ATP synthase. *Biochim. Biophys. Acta Bioenerg.* **2006**, *1757*, 326–338. [[CrossRef](#)]
32. Sielaff, H.; Duncan, T.M.; Börsch, M. The regulatory subunit ε in Escherichia coli F0F1-ATP synthase. *Biochim. Biophys. Acta Bioenerg.* **2018**, *1859*, 775–788. [[CrossRef](#)]
33. Zarco-Zavala, M.; Mendoza-Hoffmann, F.; García-Trejo, J.J. Unidirectional regulation of the F1FO-ATP synthase nanomotor by the ζ pawl-ratchet inhibitor protein of *Paracoccus denitrificans* and related α-proteobacteria. *Biochim. Biophys. Acta Bioenerg.* **2018**, *1859*, 762–774. [[CrossRef](#)] [[PubMed](#)]
34. Bhat, A.S.; Dustin Schaeffer, R.; Kinch, L.; Medvedev, K.E.; Grishin, N.V. Recent advances suggest increased influence of selective pressure in allostery. *Curr. Opin. Struct. Biol.* **2020**, *62*, 183–188. [[CrossRef](#)] [[PubMed](#)]
35. Lu, S.; Shen, Q.; Zhang, J. Allosteric Methods and Their Applications: Facilitating the Discovery of Allosteric Drugs and the Investigation of Allosteric Mechanisms. *Acc. Chem. Res.* **2019**, *52*, 492–500. [[CrossRef](#)] [[PubMed](#)]
36. Chatzigoulas, A.; Cournia, Z. Rational design of allosteric modulators: Challenges and successes. *WIREs Comput. Mol. Sci.* **2021**, *11*, e1529. [[CrossRef](#)]

37. Walker, J.E.; Saraste, M.; Runswick, M.J.; Gay, N.J. Distantly related sequences in the α - and β -subunits of ATP synthase, myosin, kinases and other ATP-requiring enzymes and a common nucleotide binding fold. *EMBO J.* **1982**, *1*, 945–951. [[CrossRef](#)]
38. Leipe, D.D.; Koonin, E.V.; Aravind, L. Evolution and classification of P-loop kinases and related proteins. *J. Mol. Biol.* **2003**, *333*, 781–815. [[CrossRef](#)]
39. Nussinov, R.; Tsai, C.-J. The Different Ways through Which Specificity Works in Orthosteric and Allosteric Drugs. *Curr. Pharm. Des.* **2012**, *18*, 1311–1316. [[CrossRef](#)]
40. Hotra, A.; Ragunathan, P.; Shuyi-Ng, P.; Seankongsuk, P.; Harikishore, A.; Sarathy, J.-P.; Saw, W.-G.; Lakshmanan, U.; Sae-Lao, P.; Kalia, N.-P.; et al. Discovery of a novel Mycobacterial F-ATP synthase inhibitor and its potency in combination with diarylquinolines. *Angew. Chemie—Int. Ed.* **2020**, *59*, 13295–13304. [[CrossRef](#)]
41. Saw, W.G.; Wu, M.L.; Ragunathan, P.; Biuković, G.; Lau, A.M.; Shin, J.; Harikishore, A.; Cheung, C.Y.; Hards, K.; Sarathy, J.P.; et al. Disrupting coupling within mycobacterial F-ATP synthases subunit ϵ causes dysregulated energy production and cell wall biosynthesis. *Sci. Rep.* **2019**, *9*, 1–15. [[CrossRef](#)]
42. Ma, Y.-X.; Wang, C.-Y.; Li, Y.-Y.; Li, J.; Wan, Q.-Q.; Chen, J.-H.; Tay, F.R.; Niu, L.-N. Considerations and Caveats in Combating ESKAPE Pathogens against Nosocomial Infections. *Adv. Sci.* **2020**, *7*, 1901872. [[CrossRef](#)]
43. Alvarez-Garcia, D.; Barril, X. Molecular simulations with solvent competition quantify water displaceability and provide accurate interaction maps of protein binding sites. *J. Med. Chem.* **2014**, *57*, 8530–8539. [[CrossRef](#)]
44. Ruiz-Carmona, S.; Alvarez-Garcia, D.; Foloppe, N.; Garmendia-Doval, A.B.; Juhos, S.; Schmidtke, P.; Barril, X.; Hubbard, R.E.; Morley, S.D. rDock: A Fast, Versatile and Open Source Program for Docking Ligands to Proteins and Nucleic Acids. *PLoS Comput. Biol.* **2014**, *10*, e1003571. [[CrossRef](#)] [[PubMed](#)]
45. Ruiz-Carmona, S.; Schmidtke, P.; Luque, F.J.; Baker, L.; Matassova, N.; Davis, B.; Roughley, S.; Murray, J.; Hubbard, R.; Barril, X. Dynamic undocking and the quasi-bound state as tools for drug discovery. *Nat. Chem.* **2017**, *9*, 201–206. [[CrossRef](#)] [[PubMed](#)]
46. Ruiz-Blanco, Y.B.; Ávila-Barrientos, L.P.; Hernández-García, E.; Antunes, A.; Agüero-Chapin, G.; García-Hernández, E. Engineering protein fragments via evolutionary and protein–protein interaction algorithms: De novo design of peptide inhibitors for FOF1-ATP synthase. *FEBS Lett.* **2021**, *595*, 183–194. [[CrossRef](#)]
47. Krah, A.; Zarco-Zavala, M.; McMillan, D.G.G. Insights into the regulatory function of the ϵ subunit from bacterial F-type ATP synthases: A comparison of structural, biochemical and biophysical data. *Open Biol.* **2018**, *8*, 170275. [[CrossRef](#)] [[PubMed](#)]
48. Shoghi, E.; Fuguet, E.; Bosch, E.; Ràfols, C. Solubility-pH profiles of some acidic, basic and amphoteric drugs. *Eur. J. Pharm. Sci.* **2013**, *48*, 291–300. [[CrossRef](#)] [[PubMed](#)]
49. Miller, B.R.; McGee, T.D.; Swails, J.M.; Homeyer, N.; Gohlke, H.; Roitberg, A.E. MMPBSA.py: An Efficient Program for End-State Free Energy Calculations. *J. Chem. Theory Comput.* **2012**, *8*, 3314–3321. [[CrossRef](#)] [[PubMed](#)]
50. Wang, E.; Sun, H.; Wang, J.; Wang, Z.; Liu, H.; Zhang, J.Z.H.; Hou, T. End-Point Binding Free Energy Calculation with MM/PBSA and MM/GBSA: Strategies and Applications in Drug Design. *Chem. Rev.* **2019**, *119*, 9478–9508. [[CrossRef](#)] [[PubMed](#)]
51. Liu, K.; Kokubo, H. Exploring the Stability of Ligand Binding Modes to Proteins by Molecular Dynamics Simulations: A Cross-docking Study. *J. Chem. Inf. Model.* **2017**, *57*, 2514–2522. [[CrossRef](#)]
52. Stoye, J.; Evers, D.; Meyer, F. Rose: Generating sequence families. *Bioinformatics* **1998**, *14*, 157–163. [[CrossRef](#)]
53. Romero-Molina, S.; Ruiz-Blanco, Y.B.; Harms, M.; Münch, J.; Sanchez-Garcia, E. PPI-Detect: A support vector machine model for sequence-based prediction of protein-protein interactions. *J. Comput. Chem.* **2019**, *40*, 1233–1242. [[CrossRef](#)]
54. Bateman, A.; Martin, M.-J.; Orchard, S.; Magrane, M.; Agivetova, R.; Ahmad, S.; Alpi, E.; Bowler-Barnett, E.H.; Britto, R.; Bursteinas, B.; et al. UniProt: The universal protein knowledgebase in 2021. *Nucleic Acids Res.* **2021**, *49*, D480–D489. [[CrossRef](#)]
55. Katoh, K. MAFFT: A novel method for rapid multiple sequence alignment based on fast Fourier transform. *Nucleic Acids Res.* **2002**, *30*, 3059–3066. [[CrossRef](#)]
56. Lu, S.; Wang, J.; Chitsaz, F.; Derbyshire, M.K.; Geer, R.C.; Gonzales, N.R.; Gwadz, M.; Hurwitz, D.I.; Marchler, G.H.; Song, J.S.; et al. CDD/SPARCLE: The conserved domain database in 2020. *Nucleic Acids Res.* **2020**, *48*, D265–D268. [[CrossRef](#)] [[PubMed](#)]
57. Gasteiger, E.; Hoogland, C.; Gattiker, A.; Duvaud, S.; Wilkins, M.R.; Appel, R.D.; Bairoch, A. Protein Identification and Analysis Tools on the ExPASy Server. In *The Proteomics Protocols Handbook*; Humana Press: Totowa, NJ, USA, 2005; pp. 571–607.
58. Crooks, G.E.; Hon, G.; Chandonia, J.-M.; Brenner, S.E. WebLogo: A Sequence Logo Generator. *Genome Res.* **2004**, *14*, 1188–1190. [[CrossRef](#)]
59. Sievers, F.; Wilm, A.; Dineen, D.; Gibson, T.J.; Karplus, K.; Li, W.; Lopez, R.; McWilliam, H.; Remmert, M.; Söding, J.; et al. Fast, scalable generation of high-quality protein multiple sequence alignments using Clustal Omega. *Mol. Syst. Biol.* **2011**, *7*, 539. [[CrossRef](#)] [[PubMed](#)]
60. Mao, H.Z.; Abraham, C.G.; Krishnakumar, A.M.; Weber, J. A functionally important hydrogen-bonding network at the betaDP/alphaDP interface of ATP synthase. *J. Biol. Chem.* **2008**, *283*, 24781–24788. [[CrossRef](#)] [[PubMed](#)]
61. Mnatsakanyan, N.; Krishnakumar, A.M.; Suzuki, T.; Weber, J. The role of the betaDELSEED-loop of ATP synthase. *J. Biol. Chem.* **2009**, *284*, 11336–11345. [[CrossRef](#)]
62. Livingstone, C.D.; Barton, G.J. Protein sequence alignments: A strategy for the hierarchical analysis of residue conservation. *Comput. Appl. Biosci.* **1993**, *9*, 745–756. [[CrossRef](#)]
63. Diacon, A.H.; Donald, P.R.; Pym, A.; Grobusch, M.; Patientia, R.F.; Mahanyele, R.; Bantubani, N.; Narasimooloo, R.; De Marez, T.; van Heeswijk, R.; et al. Randomized pilot trial of eight weeks of bedaquiline (TMC207) treatment for multidrug-resistant

- tuberculosis: Long-term outcome, tolerability, and effect on emergence of drug resistance. *Antimicrob. Agents Chemother.* **2012**, *56*, 3271–3276. [[CrossRef](#)]
64. Langlois, J.-P.; Millete, G.; Guay, I.; Dubé-Duquette, A.; Chamberland, S.; Jacques, P.-É.; Rodrigue, S.; Bourab, K.; Marsault, É. Malo Bactericidal Activity of the Bacterial ATP Synthase Inhibitor Tomatidine and the Combination of Tomatidine and Aminoglycoside Against Persistent and Virulent Forms of *Staphylococcus aureus*. *Front. Microbiol.* **2020**, *11*, 1–14. [[CrossRef](#)] [[PubMed](#)]
65. Vestergaard, M.; Roshanak, S.; Ingmer, H. Targeting the ATP Synthase in *Staphylococcus aureus* Small Colony Variants, *Streptococcus pyogenes* and Pathogenic Fungi. *Antibiotics* **2021**, *10*, 376. [[CrossRef](#)] [[PubMed](#)]
66. Milgrom, Y.M.; Duncan, T.M. F-ATP-ase of *Escherichia coli* membranes: The ubiquitous MgADP-inhibited state and the inhibited state induced by the ϵ -subunit's C-terminal domain are mutually exclusive. *Biochim. Biophys. Acta Bioenerg.* **2020**, *1861*, 148189. [[CrossRef](#)] [[PubMed](#)]
67. García-Aguilar, A.; Cuezva, J.M. A Review of the Inhibition of the Mitochondrial ATP Synthase by IF1 in vivo: Reprogramming Energy Metabolism and Inducing Mitohormesis. *Front. Physiol.* **2018**, *9*, 1322. [[CrossRef](#)] [[PubMed](#)]
68. Miranda-Astudillo, H.; Zarco-Zavala, M.; García-Trejo, J.J.; González-Halphen, D. Regulation of bacterial ATP synthase activity: A gear-shifting or a pawl-ratchet mechanism? *FEBS J.* **2021**, *288*, 3159–3163. [[CrossRef](#)]
69. Syed, H.; Tauseef, M.; Ahmad, Z. A connection between antimicrobial properties of venom peptides and microbial ATP synthase. *Int. J. Biol. Macromol.* **2018**, *119*, 23–31. [[CrossRef](#)]
70. Alvarez-Garcia, D.; Barril, X. Relationship between Protein Flexibility and Binding: Lessons for Structure-Based Drug Design. *J. Chem. Theory Comput.* **2014**, *10*, 2608–2614. [[CrossRef](#)] [[PubMed](#)]
71. Ahmad, Z.; Okafor, F.; Azim, S.; Laughlin, T.F. ATP synthase: A molecular therapeutic drug target for antimicrobial and antitumor peptides. *Curr. Med. Chem.* **2013**, *20*, 1956–1973. [[CrossRef](#)] [[PubMed](#)]
72. Talibov, V.O.; Fabini, E.; FitzGerald, E.A.; Tedesco, D.; Cederfeldt, D.; Talu, M.J.; Rachman, M.M.; Mihalic, F.; Manoni, E.; Naldi, M.; et al. Discovery of an Allosteric Ligand Binding Site in SMYD3 Lysine Methyltransferase. *ChemBioChem* **2021**, *22*, 1597–1608. [[CrossRef](#)]
73. Arcon, J.P.; Defelipe, L.A.; Lopez, E.D.; Burastero, O.; Modenutti, C.P.; Barril, X.; Marti, M.A.; Turjanski, A.G. Cosolvent-Based Protein Pharmacophore for Ligand Enrichment in Virtual Screening. *J. Chem. Inf. Model.* **2019**, *59*, 3572–3583. [[CrossRef](#)] [[PubMed](#)]
74. Ge, X.; Oliveira, A.; Hjort, K.; Bergfors, T.; Gutiérrez-de-Terán, H.; Andersson, D.I.; Sanyal, S.; Åqvist, J. Inhibition of translation termination by small molecules targeting ribosomal release factors. *Sci. Rep.* **2019**, *9*, 15424. [[CrossRef](#)] [[PubMed](#)]
75. Subiros-Funosas, R.; Ho, V.C.L.; Barth, N.D.; Mendive-Tapia, L.; Pappalardo, M.; Barril, X.; Ma, R.; Zhang, C.-B.; Qian, B.-Z.; Sintes, M.; et al. Fluorogenic Trp(redBODIPY) cyclopeptide targeting keratin 1 for imaging of aggressive carcinomas. *Chem. Sci.* **2020**, *11*, 1368–1374. [[CrossRef](#)] [[PubMed](#)]
76. Defelipe, L.; Arcon, J.; Modenutti, C.; Marti, M.; Turjanski, A.; Barril, X. Solvents to Fragments to Drugs: MD Applications in Drug Design. *Molecules* **2018**, *23*, 3269. [[CrossRef](#)] [[PubMed](#)]
77. Barril, X. Computer-aided drug design: Time to play with novel chemical matter. *Expert Opin. Drug Discov.* **2017**, *12*, 977–980. [[CrossRef](#)] [[PubMed](#)]
78. Rachman, M.; Bajusz, D.; Hetényi, A.; Scarpino, A.; Meró, B.; Egyed, A.; Buday, L.; Barril, X.; Keserú, G.M. Discovery of a novel kinase hinge binder fragment by dynamic undocking. *RSC Med. Chem.* **2020**, *11*, 552–558. [[CrossRef](#)] [[PubMed](#)]
79. Wang, Y.; Xiao, J.; Suzek, T.O.; Zhang, J.; Wang, J.; Zhou, Z.; Han, L.; Karapetyan, K.; Dracheva, S.; Shoemaker, B.A.; et al. PubChem's BioAssay Database. *Nucleic Acids Res.* **2012**, *40*, D400. [[CrossRef](#)]
80. Gledhill, J.R.; Montgomery, M.G.; Leslie, A.G.W.; Walker, J.E. Mechanism of inhibition of bovine F1-ATPase by resveratrol and related polyphenols. *Proc. Natl. Acad. Sci. USA* **2007**, *104*, 13632–13637. [[CrossRef](#)]
81. Luo, M.; Zhou, W.; Patel, H.; Srivastava, A.P.; Symersky, J.; Bonar, M.M.; Faraldo-Gómez, J.D.; Liao, M.; Mueller, D.M. Bedaquiline inhibits the yeast and human mitochondrial ATP synthases. *Commun. Biol.* **2020**, *3*, 452. [[CrossRef](#)]
82. Degiacomi, G.; Sammartino, J.C.; Sinigiani, V.; Marra, P.; Urbani, A.; Pasca, M.R. In vitro Study of Bedaquiline Resistance in *Mycobacterium tuberculosis* Multi-Drug Resistant Clinical Isolates. *Front. Microbiol.* **2020**, *11*, 2290. [[CrossRef](#)]
83. Lu, S.; Qiu, Y.; Ni, D.; He, X.; Pu, J.; Zhang, J. Emergence of allosteric drug-resistance mutations: New challenges for allosteric drug discovery. *Drug Discov. Today* **2020**, *25*, 177–184. [[CrossRef](#)] [[PubMed](#)]
84. Vella, P.; Rudraraju, R.S.; Lundbäck, T.; Axelsson, H.; Almqvist, H.; Vallin, M.; Schneider, G.; Schnell, R. A FabG inhibitor targeting an allosteric binding site inhibits several orthologs from Gram-negative ESKAPE pathogens. *Bioorg. Med. Chem.* **2021**, *30*, 115898. [[CrossRef](#)] [[PubMed](#)]
85. Cox, R.M.; Sourimant, J.; Toots, M.; Yoon, J.-J.; Ikegame, S.; Govindarajan, M.; Watkinson, R.E.; Thibault, P.; Makhsous, N.; Lin, M.J.; et al. Orally efficacious broad-spectrum allosteric inhibitor of paramyxovirus polymerase. *Nat. Microbiol.* **2020**, *5*, 1232–1246. [[CrossRef](#)]
86. Ketchum, C.J.; Al-Shawi, M.K.; Nakamoto, R.K. Intergenic suppression of the gammaM23K uncoupling mutation in F0F1 ATP synthase by betaGlu-381 substitutions: The role of the beta380DELSEED386 segment in energy coupling. *Biochem. J.* **1998**, *330*, 707–712. [[CrossRef](#)]
87. Hara, K.Y.; Noji, H.; Bald, D.; Yasuda, R.; Kinosita, K.; Yoshida, M. The role of the DELSEED motif of the beta subunit in rotation of F1-ATPase. *J. Biol. Chem.* **2000**, *275*, 14260–14263. [[CrossRef](#)] [[PubMed](#)]
88. Hara, K.Y.; Kato-Yamada, Y.; Kikuchi, Y.; Hisabori, T.; Yoshida, M. The role of the betaDELSEED motif of F1-ATPase: Propagation of the inhibitory effect of the epsilon subunit. *J. Biol. Chem.* **2001**, *276*, 23969–23973. [[CrossRef](#)]

89. Scanlon, J.A.B.; Al-Shawi, M.K.; Nakamoto, R.K. A rotor-stator cross-link in the F₁-ATPase blocks the rate-limiting step of rotational catalysis. *J. Biol. Chem.* **2008**, *283*, 26228–26240. [[CrossRef](#)] [[PubMed](#)]
90. Mnatsakanyan, N.; Kemboi, S.K.; Salas, J.; Weber, J. The beta subunit loop that couples catalysis and rotation in ATP synthase has a critical length. *J. Biol. Chem.* **2011**, *286*, 29788–29796. [[CrossRef](#)] [[PubMed](#)]
91. Tanigawara, M.; Tabata, K.V.; Ito, Y.; Ito, J.; Watanabe, R.; Ueno, H.; Ikeguchi, M.; Noji, H. Role of the DELSEED loop in torque transmission of F₁-ATPase. *Biophys. J.* **2012**, *103*, 970–978. [[CrossRef](#)] [[PubMed](#)]
92. Watanabe, R.; Koyasu, K.; You, H.; Tanigawara, M.; Noji, H. Torque transmission mechanism via DELSEED loop of F₁-ATPase. *Biophys. J.* **2015**, *108*, 1144–1152. [[CrossRef](#)] [[PubMed](#)]
93. La, T.; Clark-Walker, G.D.; Wang, X.; Wilkens, S.; Chen, X.J. Mutations on the N-terminal edge of the DELSEED loop in either the α or β subunit of the mitochondrial F₁-ATPase enhance ATP hydrolysis in the absence of the central γ rotor. *Eukaryot. Cell* **2013**, *12*, 1451–1461. [[CrossRef](#)] [[PubMed](#)]
94. Salcedo, G.; Cano-Sánchez, P.; De Gómez-Puyou, M.T.M.T.; Velázquez-Campoy, A.; García-Hernández, E. Isolated noncatalytic and catalytic subunits of F₁-ATPase exhibit similar, albeit not identical, energetic strategies for recognizing adenosine nucleotides. *Biochim. Biophys. Acta Bioenerg.* **2014**, *1837*, 44–50. [[CrossRef](#)] [[PubMed](#)]
95. Rao, S.P.S.; Alonso, S.; Rand, L.; Dick, T.; Pethe, K. The protonmotive force is required for maintaining ATP homeostasis and viability of hypoxic, nonreplicating Mycobacterium tuberculosis. *Proc. Natl. Acad. Sci. USA* **2008**, *105*, 11945–11950. [[CrossRef](#)] [[PubMed](#)]
96. Nuskova, H.; Mikesova, J.; Efimova, I.; Pecinova, A.; Pecina, P.; Drahota, Z.; Houstek, J.; Mracek, T. Biochemical thresholds for pathological presentation of ATP synthase deficiencies. *Biochem. Biophys. Res. Commun.* **2020**, *521*, 1036–1041. [[CrossRef](#)] [[PubMed](#)]
97. Nesci, S.; Trombetti, F.; Algieri, C.; Pagliarani, A. A Therapeutic Role for the F₁FO-ATP Synthase. *SLAS DISCOVERY: Adv. Sci. Drug Discov.* **2019**, *24*, 893–903. [[CrossRef](#)] [[PubMed](#)]
98. Fiorillo, M.; Ózsvári, B.; Sotgia, F.; Lisanti, M.P. High ATP Production Fuels Cancer Drug Resistance and Metastasis: Implications for Mitochondrial ATP Depletion Therapy. *Front. Oncol.* **2021**, *11*, 3875. [[CrossRef](#)] [[PubMed](#)]
99. Case, D.A.; Berryman, J.T.; Betz, R.M.; Cerutti, D.S.; Cheatham, T.E., III; Darden, T.A.; Duke, R.E.; Giese, T.J.; Gohlke, H.; Goetz, A.W.; et al. *AMBER 2014*; University of California: San Francisco, CA, USA, 2014.
100. *Molecular Operating Environment (MOE), 2014.09*; Chemical Computing Group ULC: Montreal, QC, Canada, 2015.
101. Götz, A.W.; Williamson, M.J.; Xu, D.; Poole, D.; Le Grand, S.; Walker, R.C. Routine Microsecond Molecular Dynamics Simulations with AMBER on GPUs. 1. Generalized Born. *J. Chem. Theory Comput.* **2012**, *8*, 1542–1555. [[CrossRef](#)] [[PubMed](#)]
102. Salomon-Ferrer, R.; Götz, A.W.; Poole, D.; Le Grand, S.; Walker, R.C. Routine Microsecond Molecular Dynamics Simulations with AMBER on GPUs. 2. Explicit Solvent Particle Mesh Ewald. *J. Chem. Theory Comput.* **2013**, *9*, 3878–3888. [[CrossRef](#)]
103. Hahn-Herrera, O.; Salcedo, G.; Barril, X.; García-Hernández, E. Inherent conformational flexibility of F₁-ATPase α -subunit. *Biochim. Biophys. Acta Bioenerg.* **2016**, *1857*, 1392–1402. [[CrossRef](#)]
104. Roe, D.R.; Cheatham, T.E. PTRAJ and CPPTRAJ: Software for processing and analysis of molecular dynamics trajectory data. *J. Chem. Theory Comput.* **2013**, *9*, 3084–3095. [[CrossRef](#)]
105. Pettersen, E.F.; Goddard, T.D.; Huang, C.C.; Couch, G.S.; Greenblatt, D.M.; Meng, E.C.; Ferrin, T.E. UCSF Chimera—A visualization system for exploratory research and analysis. *J. Comput. Chem.* **2004**, *25*, 1605–1612. [[CrossRef](#)]
106. Pettersen, E.F.; Goddard, T.D.; Huang, C.C.; Meng, E.C.; Couch, G.S.; Croll, T.I.; Morris, J.H.; Ferrin, T.E. UCSF ChimeraX: Structure visualization for researchers, educators, and developers. *Protein Sci.* **2020**, *30*, 70–82. [[CrossRef](#)]
107. Romero-Molina, S.; Ruiz-Blanco, Y.B.; Green, J.R.; Sanchez-Garcia, E. *ProtDCal-Suite*: A web server for the numerical codification and functional analysis of proteins. *Protein Sci.* **2019**, *28*, 1734–1743. [[CrossRef](#)]
108. Senior, A.E.; Lee, R.S.F.; Al-shawi, M.K.; Weber, J. Catalytic properties of Escherichia coli F₁-ATPase depleted of endogenous nucleotides. *Arch. Biochem. Biophys.* **1992**, *297*, 340–344. [[CrossRef](#)]
109. Van Veldhoven, P.P.; Mannaerts, G.P. Inorganic and organic phosphate measurements in the nanomolar range. *Anal. Biochem.* **1987**, *161*, 45–48. [[CrossRef](#)]
110. Kornberg, A.; Pricer, W.E. Enzymatic Phosphorylation of Adenosine and 2,6-Diaminopurine Riboside. *J. Biol. Chem.* **1951**, *193*, 481–495. [[CrossRef](#)]
111. Waterhouse, A.M.; Procter, J.B.; Martin, D.M.A.; Clamp, M.; Barton, G.J. Jalview Version 2—A multiple sequence alignment editor and analysis workbench. *Bioinformatics* **2009**, *25*, 1189–1191. [[CrossRef](#)]
112. Bowler, M.W.; Montgomery, M.G.; Leslie, A.G.W.; Walker, J.E. Ground state structure of F₁-ATPase from bovine heart mitochondria at 1.9 Å resolution. *J. Biol. Chem.* **2007**, *282*, 14238–14242. [[CrossRef](#)] [[PubMed](#)]